Journal Name

ARTICLE

Upconversion Nanoparticles for Sensing pH

Evaline S. Tsai,[a] Sandy F. Himmelstoß,[b] Lisa M. Wiesholler,[b] Thomas Hirsch,[b] and Elizabeth A.H. Hall*[a]

Received 00th January 20xx,
Accepted 00th January 20xx

DOI: 10.1039/x0xx00000x

www.rsc.org/

Upconversion nanoparticles (UCNPs) can provide a vehicle for chemical imaging by coupling chemically sensitive dyes and quenchers. The mechanism for coupling of two anthraquinone dyes, Calcium Red and Alizarin Red S, was investigated as a function of pH. The green emission band of the UCNPs was quenched by a pH-dependent inner filter effect (IFE) while the red emission band remained unchanged and acted as the reference signal for ratiometric pH measurements. Contrary to previous expectation, there was little evidence for a resonance energy transfer (RET) mechanism even when the anthraquinones were attached onto the UCNPs through electrostatic attraction. Since the UCNPs are point emitters, only emitters close to the surface of the UCNP are within the expected Förster distance and UC-RET is <10%. The theoretical and experimental analysis of the interaction between UCNPs and pH-sensitive quenchers will allow the design of UCNP pH sensors for determination of pH via IFE.

Introduction

Simple traditional pH measurement has hardly changed since the first pH electrode, but the technology is not suitable when used in some aspects of pharmaceutical product design or applications in diagnostics and therapeutics. For example, many of these applications require measurement in cells, where micro and nanoscale measurement within cellular compartments is needed to give relevant information: in drug delivery in cells, such measurement is needed to ensure that lysosomal degradation of the proposed drug is avoided before it reaches its target.[1,2] Tracking the pH of endosomal/lysosomal compartments in combination with degradation studies of drugs can provide insight to critical design parameters. Moreover, structure and activity of many biomolecules per se are influenced by pH,[3] and cancer cells, for example, have been associated with acidic extracellular pH.[4]

Current conventional pH-sensitive probes include fluorescent indicators based on fluorescein, rhodamine, cyanine, boron-dipyrromethene (BODIPY), and other organic dyes.[5] These dyes can be attached to or incorporated in nanoparticles with increased local brightness to enable ratiometric measurements and targeted delivery.[5,6] Du *et al*.[7] covalently linked fluorescein isothiocyanate (FITC) to a carbon-dot to create a ratiometric nanosensor that was used to visualize pH evolution in the endocytic pathway in real time. Burns *et al*.[8] coated a reference-dye-rich core with a thin layer of sensor-dye-rich silica. In their design, fluorescein's (λ_{ex} = 488 nm, λ_{em} = 520 nm) quantum efficiency changed with pH while tetramethylrhodamine (λ_{ex} = 540 nm, λ_{em} = 575 nm) acted as the internal standard. They were able to obtain ratiometric imaging of pH in various intracellular compartments with high spatial resolution. In another approach, Ruedas-Rama and Hall[9] attached pH-dependent anthraquinones to semiconductor quantum dots (QDs) for their nanosensor. Two of the anthraquinone derivatives, alizarin red S (ARS) and calcium red (CaR), were shown to emit light, based on energy transfer from the QDs.

However, the pH nanosensors above all suffer from autofluorescence in biological samples because their excitation in the UV or visible light range overlaps strongly with the absorbance spectra of tissue.[10] Excitation of the dye is also inefficient due to low penetration at the wavelengths used. Photobleaching is another common problem that shortens their effective "survival time" for measurement.[5] This is especially problematic in sensors because, as an indicator, the dye may need to remain photostable under repeated use for long periods of time.

Some of these drawbacks may be avoided by taking advantage of near-infrared (NIR) excitation. If the pH-sensitive probe accepts energy from upconversion nanoparticles (UCNPs) that are excited by NIR light, this would enable deep penetration in biological tissue, negligible background fluorescence, and high signal-to-noise ratios.[11] A widely used photon upconverting material is $NaYF_4$ doped with Yb as the sensitizer and Er as the activator.[12] Upon excitation with a 980 nm laser, two luminescence bands in the green (~540 nm) and red (~650 nm) region are emitted.[13] The synthesis of these UCNPs is quite versatile: the size can be tuned down to 5 nm[14] and the surface can be modified to target certain types of cells.[15,16]

Recently, studies have begun to explore the use of UCNPs for measurements of pH. One such system based on upconversion

[a] Department of Chemical Engineering and Biotechnology, University of Cambridge, Philippa Fawcett Drive, Cambridge CB3 0AS, United Kingdom. E-mail: lisa.hall@biotech.cam.ac.uk
[b] Institute of Analytical Chemistry, Chemo- and Biosensors, University of Regensburg, Regensburg 93040, Germany.
†Electronic Supplementary Information (ESI) available. See DOI: 10.1039/x0xx00000x

luminescence was developed by Sun *et al*.[17] They incorporated upconversion nanorods and bromothymol blue in a sensor film made of biocompatible polyurethane hydrogel; the film was responsive from pH 6 to 10 but not suitable for intracellular or *in vivo* measurements. Arppe *et al*.[18] designed a pH-sensitive upconverting nanoprobe that linked pHrodo Red to aminosilane-coated UCNPs to qualitatively evaluate pH in HeLa cells, determining whether certain microenvironments experienced lower pHs than others. The sensitized red emission of the pHrodo Red was too weak for quantitative analysis, but in a subsequent paper from the same group, Näreoja *et al*.[19] achieved higher loading by using the abundance of amino groups in polyethylenimine (PEI) to couple the dye. They assigned an upconversion resonance energy transfer (UC-RET) mechanism to the system, although they were not able to exclude photon reabsorption. They were then able to study membrane trafficking and its associated pH changes.

Studies on UCNPs and pH-sensitive dye combinations are focusing on their potential use in buffer solution and for intracellular measurement, but the interaction between UCNPs and different pH indicator dyes still requires further characterization. Here, we investigate the pH-dependent effect of CaR and ARS on UCNPs. CaR and ARS are interesting since they are anthraquinones with absorption bands that have strong overlap with the green emission of $NaYF_4$: Yb, Er particles. This offers a new opportunity to improve pH measurement through UCNP coupling partners and investigate the presence of inner filter effect (IFE) and resonance energy transfer (RET) mechanisms.

Experimental

Materials

Yttrium chloride hexahydrate and ytterbium chloride hexahydrate (both >99.9%) were purchased from Treibacher Industrie AG. Oleic acid and 1-octadecene (both 90%) were obtained from Alfa Aesar. Ammonium fluoride, erbium chloride hexahydrate (99.99%), sodium hydroxide, poly(isobutylene-*alt*-maleic anhydride) (PMA) (average M_w ~6 kDa), dodecylamine (98%), PEI (branched, average M_w ~25 kDa), nitrosyl tetrafluoroborate ($NOBF_4$) (95%), 4-amino-1,3-dihydroxy-anthraquinone-2-sulfonic acid (calcium red) (CaR), 3,4-dihydroxy-anthraquinone-2-sulfonic acid (alizarin red S) (ARS), citric acid monohydrate, and disodium phosphate heptahydrate were purchased from Sigma-Aldrich. All other chemicals were purchased from Sigma-Aldrich, Merck, or Acros.

Characterization Methods

Transmission electron microscopy (TEM) of UCNPs was carried out with a 120 kV Philips CM12 transmission electron microscope (FEI). The obtained images of the UCNPs were analyzed with the software ImageJ (NIH). Dynamic light scattering and ζ-potential measurements were performed with a Zetasizer Nano ZS (Malvern) at a constant temperature of 20 °C. An inductively coupled plasma optical emission spectrometer (ICP-OES) (Spectro) was used for the concentration determination of the nanoparticles. For the measurement of X-ray diffraction (XRD) patterns, a STADI P diffractometer (STOE) equipped with a Mythen 1K detector (Dectris) with a resolution of 0.005° (2θ) and a monochromatized Cu Kα1 radiation (λ = 1.54056 Å) was used.

Absorption measurements were performed at room temperature with a Lambda 14P UV/VIS spectrometer (PerkinElmer) or Synergy HT (BioTek). Luminescence spectra for the quenching experiments were obtained with an AMINCO-Bowman Series 2 luminescence spectrometer (formerly from Thermo Fisher) in which an external cw 980 nm laser module (focusable, 200 mW) (Picotronic) was installed. Luminescence spectra for the pH titration experiments were obtained with a USB4000-FL spectrometer (Ocean Optics) excited at 980 nm with a Spectra-Physics Mai Tai Ti:Sapphire NIR/IR laser (Newport) and protected with a 750 nm shortpass filter (Thorlabs). All spectra were recorded at room temperature.

Despite both instruments having a 980nm excitation, the filters did not have identical properties and it should be noted that the green/red ratio of the emission spectra was dependent on the experimental setup. For the same batch of UCNPs, the green/red ratio of UCNP luminescence is higher when measured with the AMINCO-Bowman Series 2 spectrometer compared to the USB4000-FL spectrometer (Figure S1†). In view of this difference the instrument is mentioned in the legend and base-line ratios between the green and red emissions noted for individual batches and instruments.

For lifetime measurements, a setup consisting of a 980 nm cw laser module (200 mW) (Picotronic) and an optical chopper (MC2000 with two slot chopper blade MC1F2) (Thorlabs) was used. The signal was amplified by a photomultiplier tube (PreSens) and analyzed with a digital storage oscilloscope (DSO 8204) (Voltcraft). Optical bandpass filters (FF01-535/150-25 and FF01-665/150-25) (Semrock) were used for measuring luminescence decays of the green and red upconversion emission bands.

Synthesis of UCNPs

Oleate-capped $NaYF_4$: 20% Yb, 2% Er@$NaYF_4$ nanocrystals were synthesized according to a previously described procedure.[20,21] The molar doping ratio of 20% Yb and 2% Er was selected due to its well-established usage in literature.[22,23] To synthesize core-shell UCNPs, the core material (β-$NaYF_4$: Yb, Er particles) and shell precursor (α-$NaYF_4$ particles) were synthesized separately. An additional reaction step added the shell precursor to the core material to produce core-shell particles. Detailed descriptions of these synthesis steps are presented in the ESI.†

Because spectral variations arise from differences in lanthanide distributions or surface defects from batch to batch,[20,24] the same batch of UCNPs was used within each experiment for consistency. Figure S2† shows the difference between two batches of UCNPs synthesized under the same reaction conditions. The UCNPs used for the ARS titration experiments have a slight shoulder at 555 nm, which is less prominent in the UCNPs used for the CaR titration experiments.

Surface Modification of the UCNPs

Surface Modification for Uncapped UCNPs.
Hydrophobic, oleate-coated upconversion nanoparticles were rendered water dispersible by a two-step ligand exchange. In the first step, the oleic acid was removed via $NOBF_4$.[25] Thereafter, the nanoparticles were dispersed in a two-phase system (equivalent volumes of cyclohexane and DMF), $NOBF_4$ (1 mg per 1 mg UCNPs) was added, and the mixture was stirred vigorously for 20 min at 30 °C.
Afterwards, the nanoparticles were transferred from the cyclohexane phase to the DMF phase whereas the free oleic acid stayed in the cyclohexane phase. The cyclohexane phase was rejected and the BF_4^- stabilized particles were precipitated with an excess of chloroform and separated by centrifugation (1000 *g*, 5 min). The resulting gel-like pellet was redispersed in DMF and washed one time with chloroform/DMF. Finally, the pellet was dispersed in the desired volume of DMF and centrifuged (1000 *g*, 3 min) to remove aggregates. The supernatant was collected and stored in the dark at 4 °C.

Surface Modification with PEI.
100 mg PEI (branched, average M_w ~25 kDa) was dissolved in 8 mL double distilled water and heated up to 50 °C under magnetic stirring. 40 mg of the uncapped UCNPs dispersed in 2 mL DMF were added dropwise. The dispersion was heated to 80 °C and stirred for 90 min under reflux. The particles were centrifuged at 21,000 *g*, washed with double distilled water, and redispersed by sonication. The washing step was repeated three times. The particles were filtered with a 220 nm PES filter. The concentration of the particles was determined by ICP-OES.

Surface Modification with PMA.
Poly(isobutylene-alt-maleic anhydride) (M_w 6000) was modified with dodecylamine side chains as reported in the literature.[26] 75 mg of the oleate-capped, core-shell nanoparticles were dispersed in 2 mL chloroform and 560 µL of the polymer solution (cM = 0.5 M) was added. The dispersion was stirred for 30 min for room temperature. Chloroform was removed with a rotary evaporator. The particles were dispersed in 15 mL NaOH solution (0.2 M), assisted by sonication. Afterwards, they were centrifuged at 21,000 *g*, washed with double distilled water, and redispersed by sonication again. This washing step was repeated three times. The particles were filtered with a 220 nm PES filter. The concentration of the particles was determined by ICP-OES.

Anthraquinone Attachment
A dispersion of PEI-modified UCNPs was added to a solution containing excess dye (0.05 mg per mg UCNP) and stirred for 15 min at room temperature. The particles were separated from the rest of the solution by centrifugation (21,000 *g*, 3 min) and washed with double distilled water until the supernatant was colorless.

Spectroscopic Measurements of UCNP-Anthraquinone Mixtures

Different concentrations of CaR or ARS in 0.2 M phosphate/citrate buffers of different pHs were added to PMA-modified UCNP (3 nm shell) solutions in water. The final concentration of UCNPs was 1 mg/mL. The pH response curve from the ratiometric measurements was obtained by fitting the data to a sigmoidal equation using Prism 8 software (GraphPad). The ratio of UCNP to dye was kept at 2.5:1 (on a mass basis) for these pH titration experiments. The concentration of CaR was 0.4 mM, and the concentration of ARS was 2 mM. UCNP-ARS mixture required a higher dye concentration to produce a measurable pH response due to the lower quenching efficiency of ARS.

Spectroscopic Measurements of UCNP-Anthraquinone Nanoconjugates

Phosphate/citrate buffers of different pHs (0.2 M) were added to UCNP-CaR or UCNP-ARS (PEI-modified, 1 nm shell) solutions in water. The pH response curve from the ratiometric measurements was obtained by fitting the data to a sigmoidal equation using Prism 8 software (GraphPad). The spectral overlap integrals of the UC-RET pairs were calculated with a|e software (FluorTools).

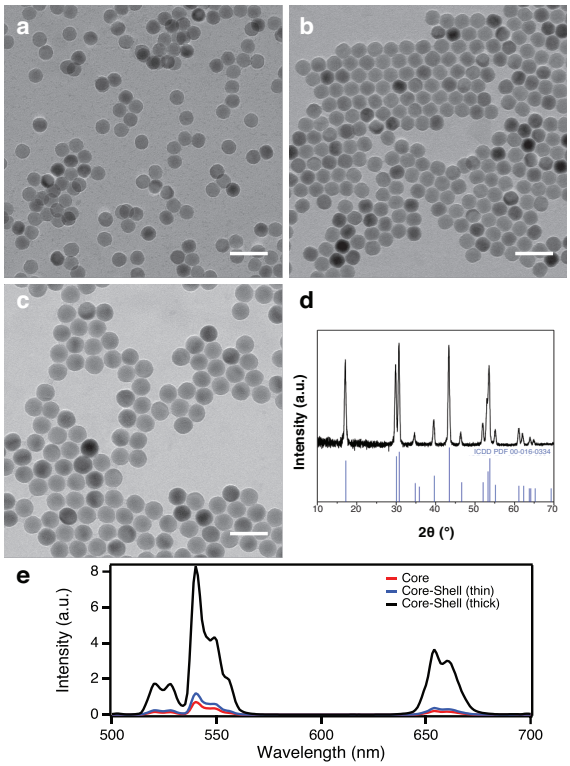

Fig. 1 TEM images of (a) core $NaYF_4$: Yb, Er particles, (b) core particles with a thin shell of $NaYF_4$, and (c) core particles with a thick shell of $NaYF_4$. The scale bars are 60 nm. Graph (d) shows the XRD pattern of (a) and the standard XRD pattern of β-$NaYF_4$. The emission spectra of core, core-shell (thin), and core-shell (thick) UCNPs are shown in (e), which were measured with an AMINCO-Bowman Series 2 spectrometer. Excitation was at 980 nm with a 200 mW cw laser.

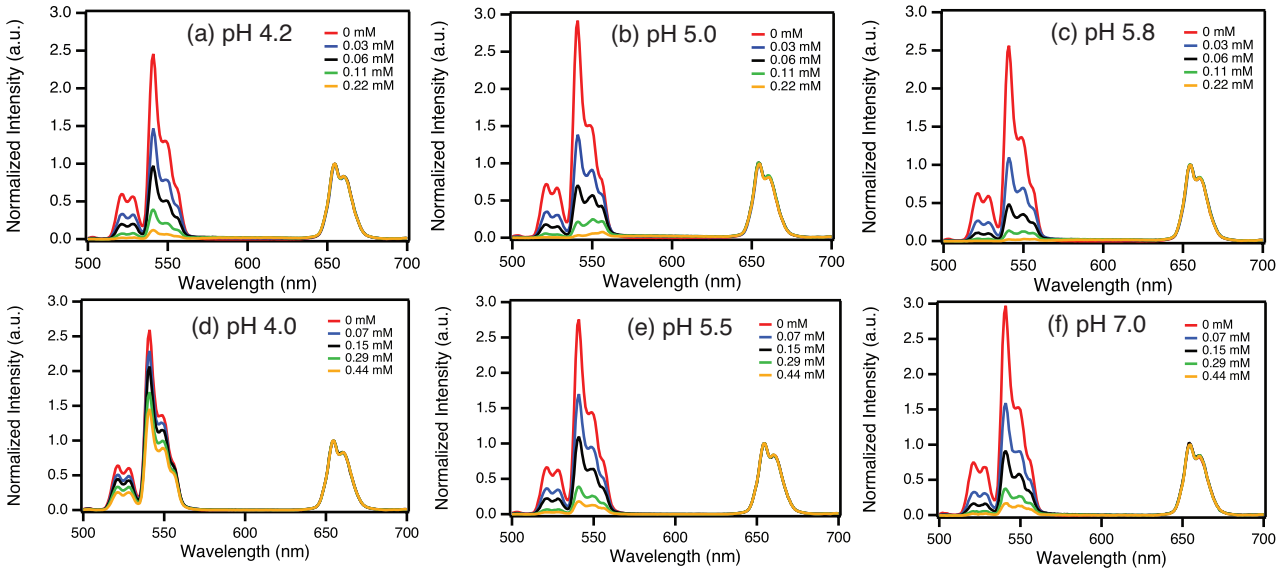

Fig. 2 Effect of different amounts of CaR on the luminescence spectra of UCNPs in phosphate/citrate buffer of different pH values: (a) 4.2, (b) 5.0, and (c) 5.8. The concentration of UCNPs was fixed at 1 mg/mL, and the concentrations of CaR were 0, 0.03, 0.06, 0.11, and 0.22 mM separately. Effect of different amounts of ARS on the luminescence spectra of UCNPs in phosphate/citrate buffer of different pH values: (d) 4.0, (e) 5.5, and (f) 7.0. The concentration of UCNPs was fixed at 1 mg/mL, and the concentrations of ARS were 0, 0.07, 0.15, 0.29, and 0.44 mM separately. Excitation was at 980 nm with a 200 mW cw laser, and emission was collected with an AMINCO-Bowman Series 2 spectrometer.

Results and Discussion

Preparation and Characterization of UCNPs

Core-only β-$NaYF_4$: Yb, Er UCNPs have very low quantum yield (QY) (<1%), so an inactive shell layer of undoped $NaYF_4$ is typically added to increase the QY by reducing surface quenching.[21,27] For our purposes, two shell thicknesses were grown: `thin' (<1 nm) and `thick' (3 nm). It is clear from the TEM images (Figure 1a-c) that a largely monodisperse population is produced in each case, with mean diameter increasing from 23.8 nm for the core to 24.6 nm for the thin shell product and 29.7 nm for the thick shell product, with a standard deviation of 1.2 nm, 0.9 nm, and 1.2 nm, respectively (Figure S3†). The core-only and core-shell UCNPs were also characterized by X-ray diffraction (XRD) (Figure 1d, S4†) and can be indexed to β-$NaYF_4$ (ICDD PDF #16-0334), confirming that the synthesis yielded a high purity hexagonal phase product.

The emission spectra for these UCNPs, excited at 980 nm, show sets of emission peaks with maxima at 540 nm and 650 nm (Figure 1e). Both types of core-shell UCNPs display greater luminescence than the core-only UCNPs because the shells reduce nonradiative vibrational deactivation processes. The thick-shell UCNPs are even brighter than the thin-shell UCNPs because the thicker shell further lengthens the distance between the luminescent centers and surface-related vibrational modes.[28]

$$E = \frac{R_0^6}{R_0^6 + r^6} \qquad (1)$$

An important requirement of UC-RET is a close-enough distance between the donor (Er^{3+}) and acceptor (dye). Theoretical calculations of RET efficiency can provide information about the feasibility of the process given a system of interest. Equation 1 shows the relationship between UC-RET efficiency (E), Förster distance (R_0), and distance between the UCNP and dye (r). Equation 2 describes the dependence of the Förster distance on various factors of the system of interest: κ^2 is the dipole orientation factor, Q_D is the quantum yield of the Er^{3+} donor, J is the spectral overlap integral of the UCNP and dye, N_A is Avogadro's number, and n is the refractive index of the medium.

$$R_0 = \sqrt[6]{\frac{9\times\ln 10\times\kappa^2\times Q_D\times J}{128\pi^5\times N_A\times n^4}} \qquad (2)$$

The Förster distance values for the UCNP/CaR and UCNP/ARS UC-RET pair combinations were estimated to be 1.78 nm and 1.52 nm, respectively, assuming a Q_D of 0.01, κ^2 of 2/3 (due to the long lifetime of UCNPs),[29] and n of 1.48 (for $NaYF_4$).[30] We calculated a J of 2.6×10^{14} nm^4 M^{-1} cm^{-1} for the UCNP/CaR pair and 1.0×10^{14} nm^4 M^{-1} cm^{-1} for the UCNP/ARS pair. The estimated value for Q_D was based on the range provided by Muhr et al.[21] and Mattsson et al. [31] Q_D is different from the overall quantum yield of the UCNP, which is much lower due to multiple possible transitions between the various lanthanide energy levels and surface quenching.[29]

For UCNP/CaR, the efficiency goes from 99+% to 4% when distance between UCNP and dye is 0.4 nm and 3 nm, respectively. Similarly for UCNP/ARS, the efficiency decreases

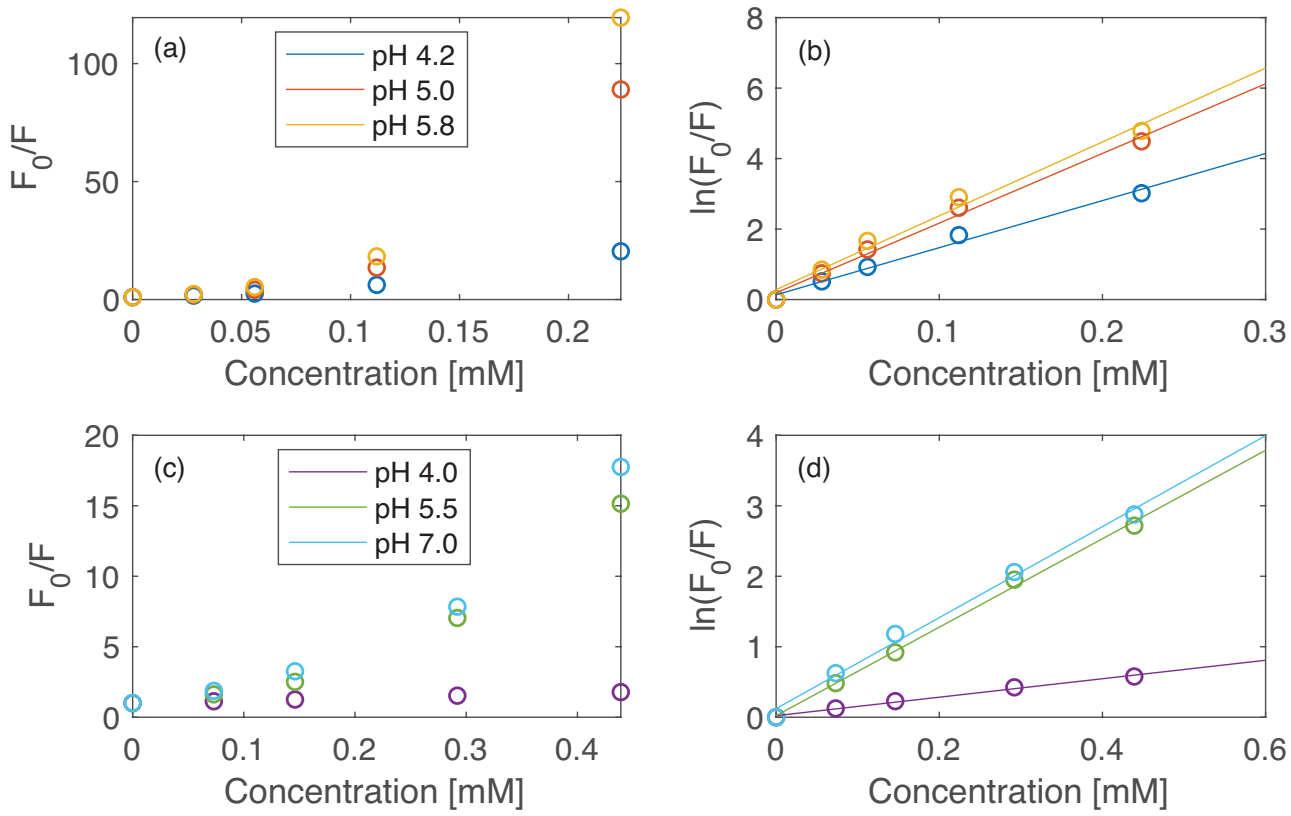

Fig. 3 Plots showing (a) Stern-Volmer quenching for UCNP-CaR, (b) Perrin model sphere of action quenching for UCNP-CaR, (c) Stern-Volmer quenching for UCNP-ARS, and (d) Perrin model sphere of action quenching for UCNP-ARS. The open circles show the quenching data, and the lines show the Perrin model fits.

from 99+% to 2% when distance is 0.4 nm versus 3 nm, respectively. Thus, potential RET mechanisms, as previously reported,[19,21] would only be expected to be suitable for the less bright thin-shell UCNPs in Figure 1b because distance between the donor (lanthanide ions) and acceptors (analyte-responsive dyes) is minimized. In contrast, the UCNPs in Figure 1c would be better matched to sensing schemes that rely on IFE due to lower anticipated energy deactivation provided by a thicker shell.[32-34]

The upconversion photoluminescence of UCNPs alone is almost independent of pH, which can be seen in Figure 2 where the ratio of the green peak at 540 nm to the red peak at 650 nm ($I_{g/r}$) is 2.7±0.2 across the 6 different pHs. However, by inclusion of pH-sensitive probes we can explore the feasibility of developing a pH sensor based on UCNPs.

UCNP Mixed with CaR and ARS in Solution

CaR and ARS are anthraquinone dyes with similar absorbance maxima in the visible light region at pH 7 (λ_{max} = 535 nm and 520 nm, respectively, Figure S5†) overlapping with the emission wavelength for the UCNPs, but different response at low pH where the ARS develops a new non-overlapping absorption maximum at 420 nm. Furthermore, the fluorescence of CaR and ARS are pH dependent. The fluorescence of CaR (λ_{ex} = 535 nm, λ_{em} = 585 nm) increases when pH is changed from 4-6 (Figure S6a†). The fluorescence of ARS is also pH dependent, but due to the absorbance wavelength shift from 420 nm (low pH) to 520 nm (high pH), the dye is almost not fluorescent at acidic pH and the intensity only increases dramatically when pH > 7 (λ_{ex} = 520 nm, λ_{em} = 555 nm, Figure S6b†).

To study the interaction between UCNPs and these anthraquinone dyes, different amounts of CaR and ARS were added into a fixed concentration of UCNP in solution. The UCNPs were modified with the amphiphilic polymer PMA to avoid direct electrostatic attraction between particle and dye. A ζ-potential measurement of -33 mV indicates the success of the surface modification with the polymer (Figure S7a†) and the colloidal stability, including the absence of particle aggregation, was confirmed by DLS (Figure S8†).

UCNPs that are functionalized with an amphiphilic coating on top of the original oleate capping are known to exhibit higher

Table 1 Fluorescence lifetimes at 540 nm of thick-shell UCNPs, UCNP-CaR mixtures, thin-shell UCNPs, and UCNP-CaR conjugates in phosphate/citrate buffer solution of different pH values

pH	τ (thick-shell UCNPs, μs)	τ (mixtures, μs)	τ (thin-shell UCNPs, μs)	τ (conjugates, μs)
4.2	270 ± 15	272 ± 1	243 ± 2	228 ± 9
5.0	274 ± 3	275 ± 8	247 ± 2	229 ± 10
5.8	274 ± 5	279 ± 7	247 ± 1	224 ± 3

$I_{g/r}$ compared to those that are surface modified through ligand exchange. This is highly beneficial for sensing applications that use the green luminescence as the analyte-dependent signal.[20] Figure 2a-c displays the normalized emission spectra of the UCNP-CaR mixtures, and a pK_a of ~5.0 is estimated from the change in absorbance at 533 nm (Figure S9a†). Without taking into account any shift in the apparent pK_a due to interactions with the PMA on the UCNP, the dye is predominantly in its protonated form at pH 4.2 and mostly unprotonated at pH 5.8.[35] In this pH range, it is clear that CaR plays a role in quenching the green emission of the UCNP, with intensity decreasing relative to the red intensity as the concentration of dye increases.

In contrast, Figure 2d-f shows the normalized emission spectra of the UCNP-ARS mixtures. Figure S9b† suggests an apparent pK_a of ~5.5 for ARS in solution measured at 518 nm (note that the shift in emission wavelength with pH (figure S6b†) truncates low pH sensitivity measured at ~520nm, so the actual pK_a for the dye may be lower). Nevertheless, it can be assumed that the dye is mostly protonated at pH 4.0 and primarily unprotonated at pH 7.0. Like CaR, higher concentration of ARS increases quenching of the green peak of the UCNP relative to the red peak, but this is less pronounced at pH 4.0.

The Stern-Volmer equation is frequently used to describe fluorescence quenching:

$$\frac{F_0}{F} = 1 + K_{SV}[Q] \qquad (3)$$

where, in this setting, F_0 and F are the fluorescence intensities of UCNPs in the absence and presence of anthraquinone dye, K_{SV} is the Stern-Volmer quenching constant, and [Q] is the concentration of CaR or ARS.[36,37]

The linear Stern-Volmer plots expected from Equation 3 are not obtained here (Figure 3a,c); instead, positive deviations are observed. Upward-curving Stern-Volmer plots can result from: static and dynamic quenching occurring simultaneously and/or "static-like" quenching due to the fluorophore's adjacency to the quencher at high concentrations.[36-38]

The most definitive method of distinguishing between the two mechanisms is to carry out fluorescence lifetime measurements.[39] Fluorescence lifetimes were measured for UCNPs at 540 nm in the absence and presence of CaR (Table 1) and ARS (Table 2). The average fluorescence lifetime at this wavelength is almost unchanged after addition of CaR or ARS in solution. For example, the lifetime of UCNP-CaR mixture is 272 μs compared to 270 μs for thick-shell UCNPs in pH 4.2 buffer solution. The overlap of the decay curves (Figure S10a-c†) also confirms this. As validation, the lifetime at 660 nm was also measured and the decay curves found to be independent of the presence or absence of dye. Additionally, there is no significant lifetime variation of the UCNP green emission across different pHs, indicating that the UCNPs are relatively stable towards pH change in this range.

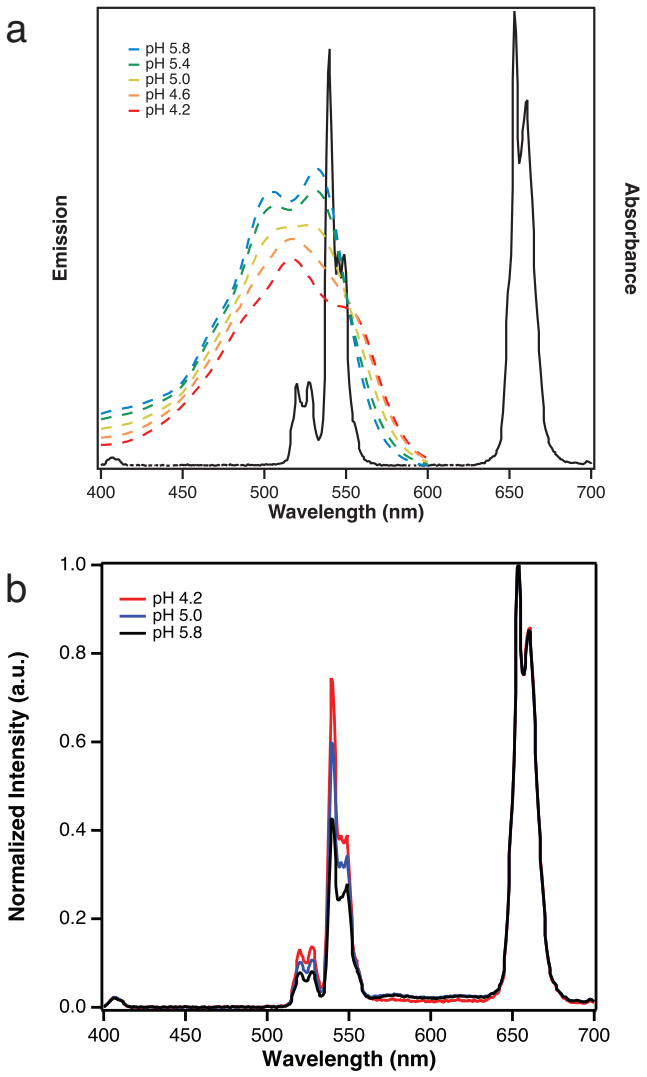

Fig. 4 (a) Absorption spectra (dashed lines in color, right y-axis) of CaR in aqueous solutions of different pHs overlaid with the emission spectrum of the UCNP in water upon 980 nm excitation (solid black line, left y-axis). (b) Normalized emission spectra of UCNP-CaR mixtures at pH 4.2, 5.0, and 5.8 collected with a USB4000-FL spectrometer upon 980 nm excitation.

These data could point to a static quenching mechanism, with a non-fluorescent ground-state complex forming between the fluorophore and quencher. Examination of the absorption spectra can determine whether such a complex exists between the UCNP and anthraquinone dye after mixing. Dynamic quenching only affects the excited state of the UCNP, so its absorption spectrum is not expected to change, while ground-state complex formation results in a new, unique absorption

Table 2 Fluorescence lifetimes at 540 nm of thick-shell UCNPs, UCNP-ARS mixtures, thin-shell UCNPs, and UCNP-ARS conjugates in phosphate/citrate buffer solution of different pH values. Different batches of UCNPs were used for the lifetime studies with the dyes in Tables 1 and 2, resulting in different lifetimes due to batch-to-batch variation

pH	τ (thick-shell UCNPs, μs)	τ (mixtures with dyes, μs)	τ (thin-shell UCNPs, μs)	τ (conjugates with dyes, μs)
4.0	161 ± 3	160 ± 6	129 ± 2	120 ± 4
5.5	157 ± 2	156 ± 17	127 ± 3	118 ± 1
7.0	162 ± 3	158 ± 8	128 ± 6	116 ± 1

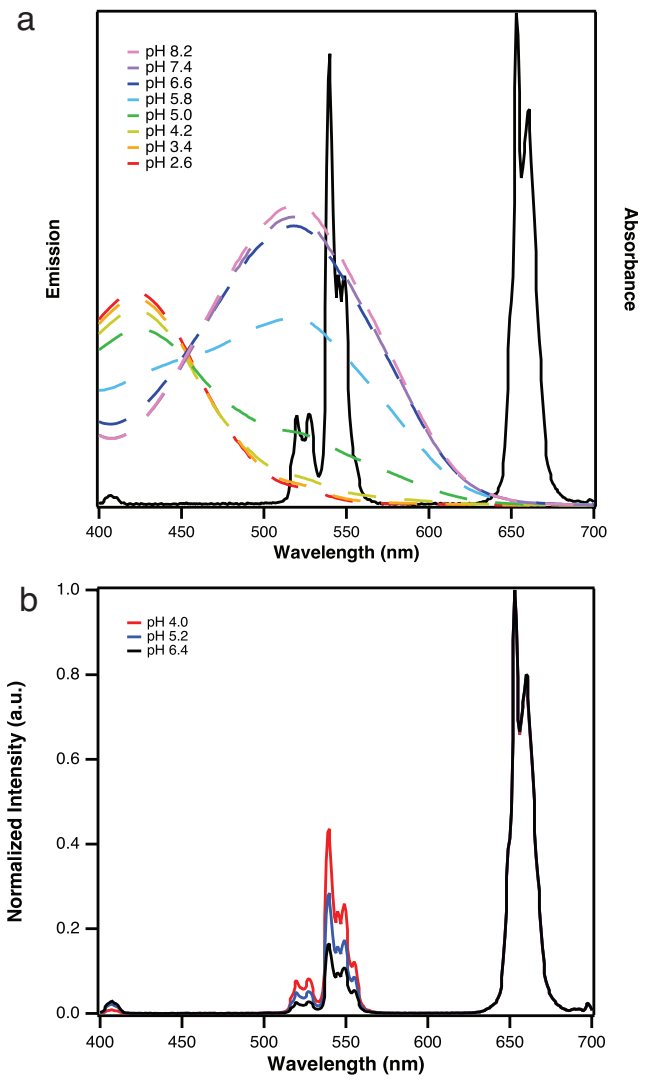

Fig. 5 (a) Absorption spectra (dashed lines in color, right y-axis) of ARS in aqueous solutions of different pHs overlaid with the emission spectrum of the UCNP in water upon 980 nm excitation (solid black line, left y-axis). (b) Normalized emission spectra of UCNP-ARS mixtures at pH 4.0, 5.2, and 6.4 collected with a USB4000-FL spectrometer upon 980 nm excitation.

spectrum.[36] Because there is no significant difference (e.g. emergence of a new peak or shoulder) between the absorption spectrum of UCNP-CaR mixture and that of the sum value of UCNP and CaR individually (Figure S11a†), we can infer that no ground-state complex formed.[40,41]

The same principle applies for UCNP-ARS mixtures (Figure S11b†). However, although the formation of a ground-state complex is ruled out, Figure 2 indicates that some sort of non-diffusional quenching is responsible for the decrease in the green luminescence intensity of the UCNP when anthraquinone dye is present. Perrin's model of static quenching does not assume complex formation; rather, there is apparent static quenching because of the proximity between the fluorophore and quencher during excitation, which results in immediate quenching that makes the pair act like a dark complex.[36,42] At high concentrations, any quencher molecule found within a sphere-of-action is deactivated instantaneously with probability of unity, and those outside the volume do not participate in quenching.[42,43] Because of this, $\tau = 0$ inside V and $\tau = \tau_0$ outside V, which is consistent with the lack of change in lifetime for non-diffusional quenching.[43] There have been multiple reports of using the Perrin model to fit the upward curvature in Stern-Volmer plots, including systems involving small molecules as the quencher.[40,44,45]

The Perrin model without diffusional contribution has the following relationship:

$$\frac{F_0}{F} = \exp(\alpha[Q]) \qquad (4)$$

where $\alpha = N_A V$. N_A is Avogadro's number and V is the volume of the sphere-of-action.[9,40,42]

Figure 3b,d shows the fitting of the quenching data. Based on the Perrin analysis, the sphere of action, obtained from the slope of the lines, shows an increase with pH (Table 3). Larger sphere volumes represent higher efficiency of quenching.[46] This trend matches what we find in Figure 2, where quenching is greatest and the sphere of action is largest at the highest pH (for a given concentration of CaR or ARS). From this analysis, we can also see that CaR, which has larger sphere volumes, is a more efficient quencher than ARS. This is also confirmed by a higher concentration of ARS being required to obtain the same quenching effect as CaR (Figure 2).

The spectral overlap between the green band of the luminescence spectrum of UCNP and absorption spectra of CaR at different pH values explain these different pH-dependent effects (Figure 4a). The pH-independent red emission band (650 nm) of the UCNP can act as a reference signal for quantitative ratiometric measurement of pH, linked with the CaR/$CaRH^+$-dependent green luminescence of the UCNP (Figure 4b).

For ARS, the red emission band can also be used as the reference signal for quantitative measurements of pH, but only the absorption spectra of the deprotonated ARS overlaps with the green emission band of the UCNP (Figure 5a). The spectral overlap of ARS with UCNP increases with pH, causing the UCNP intensity at 540 nm to decrease relative to the intensity at 650 nm (Figure 5b).

Thus, depending on whether the anthraquinones are in their acidic form or basic form, the dyes exert an inner filter effect on the green emission of the UCNP. The absorption coefficient for the dye at the wavelength of spectral overlap increases with pH for both CaR and ARS so the IFE efficiency is higher at higher pH, resulting in a sigmoidal response curve of the relative quenching for both CaR and ARS (Figure 6a,c). The experimental pK_a calculated from the sigmoidal fit is 5.0±0.2 for the UCNP-CaR mixture, which is the same as that of the dye alone. The experimental apparent pK_a of the UCNP-ARS mixture calculated

Table 3 Radii of the quenching spheres for UCNP-CaR mixtures and UCNP-ARS mixtures

pH	*r* (UCNP-CaR, nm)	pH	*r* (UCNP-ARS, nm)
4.2	1.74	4.0	0.80
5.0	1.99	5.5	1.35
5.8	2.02	7.0	1.37

from the sigmoidal fit is 5.4±0.1, which is also similar but slightly lower than that of the dye alone, probably since no further quenching of the UCNP green emission is achieved above pH 5.5.

UCNP-CaR and UCNP-ARS Nanoconjugates

Although these data support an IFE rather than the RET mechanism proposed previously for UCNP-dye combinations, the shell thickness of 3 nm would be expected to limit RET. In contrast, the 0.4 nm shell UCNPs are less efficient emitters, but their UCNP to dye distance could potentially support RET. Furthermore, the concentration of UCNP to dye is maintained to give a reproducible green/red photoluminescence ratio at each pH (Figure 2). This can be accomplished with incorporation of both UCNP and dye in a support matrix which prevents leakage that would affect the ratio between the two components.[17]

The CaR and ARS dyes are anthraquinone derivatives with a negatively charged sulfonate group (Figure S12†), so they can be expected to form UCNP-CaR and UCNP-ARS conjugates through electrostatic interaction with a positively charged UCNP.

A two-step ligand-exchange protocol (see Experimental section) was used to modify the surface of the nanoparticles with PEI and produce a surface with abundant amino groups and positive zeta potential (+36 mV) (Figure S7b†). Because RET is highly dependent on distance, as shown by the theoretical calculations above, the dye attachment is necessary to maximize the number of dyes that are as close as possible to the near-surface Er^{3+} ions. Figure S13† also shows that the UCNPs from the surface modification form stable colloids without apparent aggregation, even at different pHs. Across two units of pH, the hydrodynamic diameter did not vary by more than 10 nm and every measured polydispersity index (PDI) was less than 0.190.

CaR attachment onto PEI-modified UCNP was easily confirmed by the pink color on the surface of the particles, after purification by redispersion-precipitation-centrifugation cycles to remove excess, non-attached dye. In the case of ARS, the color observed was purple. Although the dyes are attached to the UCNP through electrostatic attraction, which is a weaker interaction than covalent bonding, the conjugates are still quite stable and do not exhibit major leakage of the dye. Tables S1† and S2† show that the fraction of CaR and ARS remaining on the UCNP remains ~90% after each wash step.

The dye loading of CaR and ARS can be calculated from a combination of ICP and absorbance spectroscopy (see the ESI† for more details). For the same excess dye concentration (0.05 mg per mg UCNP) the UCNP-CaR conjugates have approximately 120 dye molecules per UCNP particle and the UCNP-ARS conjugates have around 1600 molecules per particle. It is anticipated that the protonated amino group of the CaR will reduce electrostatic binding to the protonated amino groups of the PEI covering the surface of the UCNPs, so the attachment is not as strong compared to that of ARS.

Figure 7a shows the normalized emission spectra of UCNP-CaR conjugates at different pHs after excitation with a 980 nm laser. In this instance, the green UCNP emission coincides well with the excitation wavelength for CaR (λ_{max} = 535 nm); there is a small decrease in the emission intensity at 540 nm but no clear evidence of UC-RET acceptor emission at 585 nm. Similarly, Figure 7b shows the normalized emission spectra of UCNP-ARS conjugates at various pHs with the same laser. In this case, the green peak of the UCNP shows a more significant decrease relative to the red peak as pH increases, likely due to the higher dye loading compared to the CaR system.

$$\mathrm{E} = 1 - \frac{\tau(UCNP-dye)}{\tau(UCNP)} \qquad (5)$$

Lifetime experiments were performed before and after dye attachment to determine whether the anthraquinones are close enough to the UCNP in this conjugate design for UC-RET to take place between the donor (UCNP) and acceptor (CaR or ARS). It is evident from Figure S10d-f† that the conjugates produce a much noisier result, probably because there are different Er^{3+} - dye distances for the Er^{3+} ions near the surface of the UCNPs and the inner Er^{3+} ions. Nevertheless, there is a decrease of 10-30 μs in the lifetime of the green emission band at 540 nm after CaR attachment (Table 1, Figure S10d-f†), with clear separation of the data <0.25ms compared with the UCNP without dye.

Table 4 Förster distances and donor quantum yields for different Er^{3+} (donor) and anthraquinone (acceptor) distances assuming a UC-RET efficiency of 0.09. 4.8 nm is the distance at which Q_D would be 100% for UCNP-CaR. 5.7 nm is the distance at which Q_D would be 100% for UCNP-ARS

r (nm)	R_0 (nm)	Q_D (UCNP-CaR)	Q_D (UCNP-ARS)
0.4	0.27	1.3×10^{-7}	3.3×10^{-7}
1	0.68	3.1×10^{-5}	8.0×10^{-5}
2	1.4	0.0020	0.0051
4	2.7	0.13	0.33
4.8	3.3	…	1.0
5.7	3.8	1.0	…

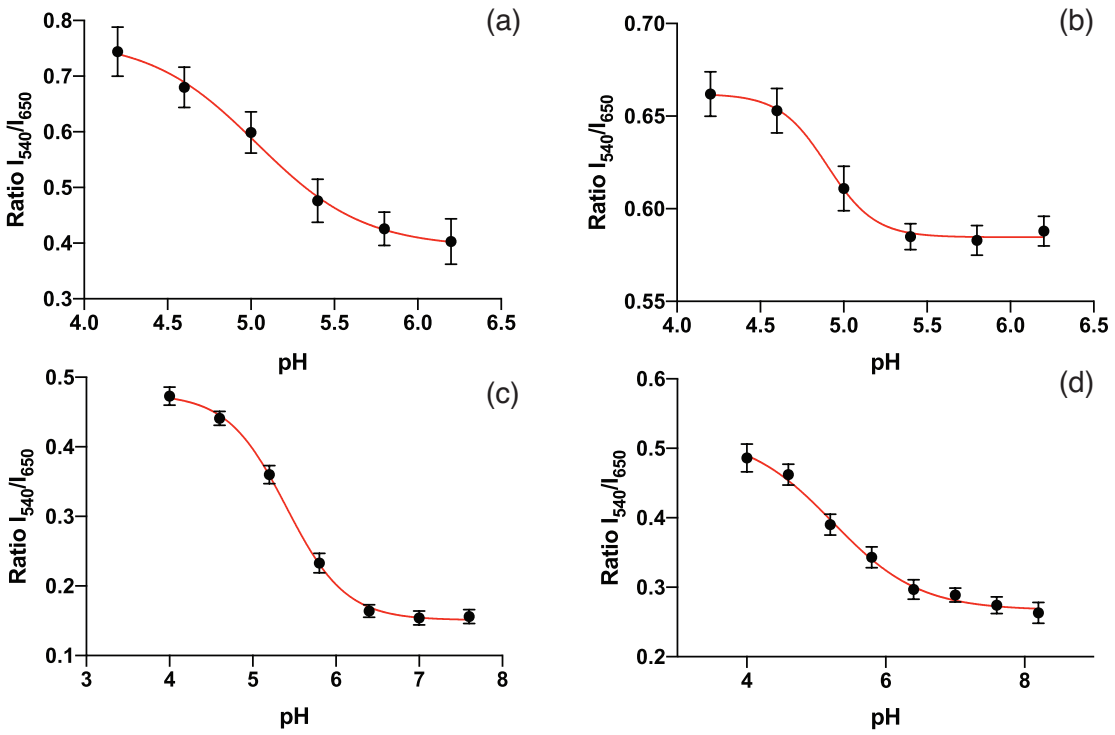

Fig. 6 Ratiometric pH-titration data measured at 540 nm and 650 nm of (a) UCNP-CaR mixture, (b) UCNP-CaR conjugate, (c) UCNP-ARS mixture, and (d) UCNP-ARS conjugate. The red lines represent the sigmoidal interpolation curves. The data were collected with a USB4000-FL spectrometer upon 980 nm excitation.

There is a more modest decrease in lifetime of the green upconversion band after ARS attachment, from 127-129 μs to 116-120 μs (Table 2). Equation 5 relates UC-RET efficiency to lifetime of the UCNP in the presence and absence of dye. From the lifetime data, UC-RET efficiencies of 4-9% for UCNP-CaR and 4-7% for UCNP-ARS are obtained. Thus, the quenching mechanism in this conjugate system can still be attributed primarily to emission-reabsorption.

Nevertheless, the UC-RET efficiencies allow us to estimate distances between donor and acceptor using Equations 1 and 2 (Table 4), the reverse of the theoretical calculations of RET efficiencies performed earlier. Based on acceptable boundary values for Q_D (on the order of 0.1% to 5%),[29,31] the UCNP-anthraquinone distances were estimated to be 1-3 nm given a UC-RET efficiency of 0.09. With a 23.8 nm UCNP core, shell thickness of 0.4 nm, and PEI thickness of 2.1±0.1 nm (from TEM), this suggests that only the Er^{3+} ions close to the surface of the UCNP, within the Förster distance, are involved in RET, while the inner Er^{3+} ions contribute to radiative energy transfer to the dyes through reabsorption.[50] Furthermore, because the polymer is not expected to form a densely packed layer due to charge repulsion from the positive amino groups on PEI,[47-49] the dyes may be able to penetrate the PEI layer and become attached by electrostatic forces within the polymer layer and not just at the surface. However, this porosity would also infer that protons diffusing into a dye-PEI matrix are in equilibrium with a PEI buffered environment, which might modulate the pH response, which could influence the apparent pK_a for the dye.

The UCNP-CaR nanosensor exhibits a dynamic range between pH ~4.6 and ~5.2. From the sigmoidal fit (Figure 6b), the experimental pK_a is 4.9±0.1, which is similar to the UCNP-CaR mixture and prior studies involving the dye,[9,51] so does not suggest that the PEI layer is having a significant buffering effect. This pH range is ideal for tracking pH in endosomes and lysosomes.[5,52] The UCNP-ARS nanoconjugate shows a wider range of pH responsiveness (Figure 6d), between pH ~4.4 and ~6.4, with pK_a of 5.4±0.4 and a similar pH sensitivity of ~0.1 ratio difference per pH unit. The behavior of this conjugate is also similar to the UCNP-ARS mixture and does not highlight any buffering effect by the PEI, which may point to just a surface loading of dye rather than penetration into the PEI layer. In this case the Förster distance will be limited by the thickness of the PEI layer and higher UC-RET efficiencies are not likely to be achieved.

Conclusions

In this work, the mechanism of coupling for two anthraquinone dyes, CaR and ARS, on UCNPs was studied. When thick-shell UCNPs and anthraquinones were mixed directly, the decrease in the green intensity of the UCNPs was due to IFE. However, when thin-shell UCNPs and anthraquinones were conjugated through electrostatic attraction with PEI coated on the particle, a low efficiency (<9%) UC-RET could occur between the UCNPs and dye, but the main quenching mechanism was still emission-reabsorption. This correlates with the point emitter character of the UCNP, so that only Er^{3+} ions close to the surface are within

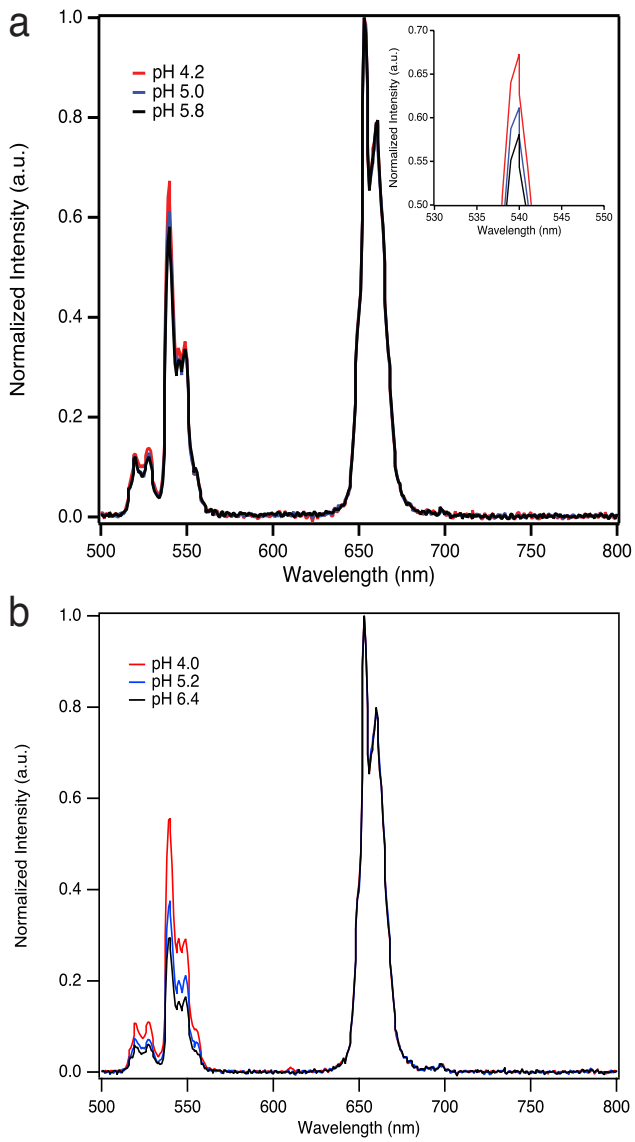

Fig. 7 (a) Normalized emission spectra of UCNP-CaR conjugates in phosphate/citrate buffer solutions of pH 4.2, 5.0, and 5.8 and (b) normalized emission spectra of UCNP-ARS conjugates in phosphate/citrate buffer solutions of pH 4.0, 5.2, and 6.4 collected with a USB4000-FL spectrometer upon 980 nm excitation.

the Förster distance for UC-RET with the dye. Some improvement might be achieved by direct attachment of the dye to the UCNP (rather than via a PEI coating), thus reducing the donor-acceptor distance and higher efficiencies could emerge from smaller UCNPs (with a higher surface:core ratio), but, this mechanism will be inherently limited in its efficiency due to spatial distribution of the point emitters and leads to the conclusion that the preferred approach is to target the IFE and design the brighter, thick-shell UCNPs.

The potential of UCNP-anthraquinone coupling was demonstrated for pH measurement, utilizing the interference free, deep penetration of the NIR excitation. The UCNP-ARS nanosensor displayed a broader range of pH response compared to the UCNP-CaR nanosensor. ARS is suitable for measurement from pH 4.4 to 6.4, while the lower CaR pK_a is better tuned to measurement of pH in lysosomes, which can reach as low as pH 4. However, CaR loading on the PEI coating of the UCNP is low, probably due to the amine group of the dye. This suggests that other anthraquinones with appropriate spectral overlap could be selected to increase sensitivity and extend the measurable pH range. The integration between the UCNP and dye through electrostatic binding has the potential for continuous sensing of pH in cells.

This study provides the framework for creating pH sensing systems using UCNPs and charged dyes based on their spectral overlap. It is critical to examine the interplay between static and dynamic energy transfer when optimizing pH sensing nanoplatforms.[53] This work shows that energy transfer mechanisms other than UC-RET dominate even when the distance between UCNP and pH dye is close.[54] As strategies to enhance the brightness of UCNPs improve, their use as probes in biosensing and other applications will increase.[55] With the adaptability of the surface chemistry of UCNPs,[56] the method introduced here can be extended to a wide range of pH-sensitive molecules with exquisite sensitivity. These quantitative titration measurements were performed using a simple spectrometer without a photomultiplier tube. A plate reader with a more sensitive detector can capture >100,000 counts for the UCNP signals at a hundredth of the concentration,[18] which would add significantly to the sensitivity and resolution of pH that are reported here.

Conflicts of interest

There are no conflicts to declare.

Acknowledgements

This work was supported by the EPSRC Cambridge NanoDTC, EP/L015978/1. The authors would like to thank Markus Buchner for assistance in surface chemistry.

Notes and references

1 H. Pan and J. Kopecek, in *Multifunctional Water-Soluble Polymers for Drug Delivery*, ed. V. Torchilin, Springer, New York, 1st edn, 2008, ch. 4, pp. 81–142.

2 R. Chen, in *Drug Delivery Systems: Advanced Technologies Potentially Applicable in Personalised Treatment*, ed. J. Coelho, Springer, Dordrecht, 1st edn, 2013, ch. 1, pp. 1–34.

3. H. Hoffmann and S. Pisch-Heberle, in *Protein Formulation and Delivery*, ed. E. J. McNally and J. E. Hastedt, CRC Press, Boca Raton, 2nd edn, 2008, ch. 4, pp. 73-108.

4 Y. Xu, J. Cui and D. Puett, *Cancer Bioinformatics*, Springer, New York, 2014.

5 J. Han and K. Burgess, *Chem. Rev.*, 2010, **110**, 2709–2728.

6 A. Schulz and C. McDonagh, *Soft Matter*, 2012, **8**, 2579–2585.

7 F. Du, Y. Ming, F. Zeng, C. Yu and S. Wu, *Nanotechnology*, 2013, **24**, 365101.

8 A. Burns, P. Sengupta, T. Zedayko, B. Baird and U. Wiesner,

Small, 2006, **2**, 723–726.
9 M. J. Ruedas-Rama and E. A. H. Hall, *Nanotechnology*, 2014, **25**, 195501.
10 T. G. Phan and A. Bullen, *Immunol. Cell Biol.*, 2010, **88**, 438–444.
11 Y. I. Park, K. T. Lee, Y. D. Suh and T. Hyeon, *Chem. Soc. Rev.*, 2015, **44**, 1302–1317.
12 M. Haase and H. Schafer, *Angew. Chem. Int. Ed.*, 2011, **50**, 5808–5829.
13 T. Cong, Y. Ding, S. Xin, X. Hong, H. Zhang and Y. Liu, *Langmuir*, 2016, **32**, 13200–13206.
14 Y. Hu, B. Wu, Q. Jin, X. Wang, Y. Li, Y. Sun, J. Huo and X. Zhao, *Talanta*, 2016, **152**, 504–512.
15 N. M. Idris, M. K. Gnanasammandhan, J. Zhang, P. C. Ho, R. Mahendran and Y. Zhang, *Nat. Med.*, 2012, **18**, 1580–1585.
16 A. B. Chinen, C. M. Guan, J. R. Ferrer, S. N. Barnaby, T. J. Merkel and C. A. Mirkin, *Chem. Rev.*, 2015, **115**, 10530–10574.
17 L.-N. Sun, H. Peng, M. I. J. Stich, D. Achatz and O. S. Wolfbeis, *Chem. Commun.*, 2009, 5000–5002.
18 R. Arppe, T. Nareoja, S. Nylund, L. Mattsson, S. Koho, J. M. Rosenholm, T. Soukka and M. Schaferling, *Nanoscale*, 2014, **6**, 6837–6843.
19 T. Nareoja, T. Deguchi, S. Christ, R. Peltomaa, N. Prabhakar, E. Fazeli, N. Perala, J. M. Rosenholm, R. Arppe, T. Soukka and M. Schaferling, *Anal. Chem.*, 2017, **89**, 1501–1508.
20 S. Wilhelm, M. Kaiser, C. Wurth, J. Heiland, C. Carrillo-Carrion, V. Muhr, O. S. Wolfbeis, W. J. Parak, U. Resch-Genger and T. Hirsch, *Nanoscale*, 2015, **7**, 1403–1410.
21 V. Muhr, C. Wurth, M. Kraft, M. Buchner, A. J. Baeumner, U. Resch-Genger and T. Hirsch, *Anal. Chem.*, 2017, **89**, 4868– 4874.
22 G. S. Yi and G. M. Chow, *Adv. Funct. Mater.*, 2006, **16**, 2324–2329.
23 J.-C. Boyer, F. Vetrone, L. A. Cuccia and J. A. Capobianco, *J. Am. Chem. Soc.*, 2006, **128**, 7444–7445.
24 J. Zhou and J. Qiu, in *Phosphors, Up Conversion Nano Particles, Quantum Dots and Their Applications*, ed. R.-S. Liu, Springer, Singapore, 2016, vol. 2, ch. 10, pp. 311-332.
25 V. Muhr, S. Wilhelm, T. Hirsch and O. S. Wolfbeis, *Acc. Chem. Res.*, 2014, **47**, 3481–3493.
26 C.-A. J. Lin, R. A. Sperling, J. K. Li, T.-Y. Yang, P.-Y. Li, M. Zanella, W. H. Chang and W. J. Parak, *Small*, 2008, **4**, 334–341.
27 J.-C. Boyer and F. C. J. M. van Veggel, *Nanoscale*, 2010, **2**, 1417–1419.
28 Y. Wang, L. Tu, J. Zhao, Y. Sun, X. Kong and H. Zhang, *J. Phys. Chem. C*, 2009, **113**, 7164–7169.
29 S. Bhuckory, E. Hemmer, Y.-T. Wu, A. Yahia-Ammar, F. Vetrone and N. Hildebrandt, *Eur. J. Inorg. Chem.*, 2017, **2017**, 5186-5195.
30. P. Kim, C. Li, R. E. Riman and J. Watkins, *ACS Appl. Mater. Interfaces*, 2018, **10**, 9038-9047.
31 L. Mattsson, K. D. Wegner, N. Hildebrandt and T. Soukka, *RSC Adv.*, 2015, **5**, 13270-13277.
32 Y. Liu, Q. Ouyang, H. Li, Z. Zhang and Q. Chen, *ACS Appl. Mater. Interfaces*, 2017, **9**, 18314–18321.
33 H. Chen and J. Ren, *Talanta*, 2012, **99**, 404–408.
34 H. Chen, A. Fang, L. He, Y. Zhang and S. Yao, *Talanta*, 2017, **164**, 580–587.
35 J. N. Aronson, *Biochem. Educ.*, 1983, **11**, 68.
36 J. R. Lakowicz, *Principles of Fluorescence Spectroscopy*, Springer, New York, 3rd edn, 2006.
37 N. Ghosh, R. Mondal and S. Mukherjee, *Langmuir*, 2015, **31**, 8074–8080.
38 J.-M. Swiecicki, F. Thiebaut, M. D. Pisa, S. Gourdin-Bertin, J. Tailhades, C. Mansuy, F. Burlina, S. Chwetzoff, G. Trugnan, G. Chassaing and S. Lavielle, *Sci. Rep.*, 2016, **6**, 1–11.
39 M. A. Omary and H. H. Patterson, in *Encyclopedia of Spectroscopy and Spectrometry*, ed. J. C. Lindon, G. E. Tranter and D. W. Koppenaal, Academic Press, Oxford, 3rd edn, 2017, vol. 2, ch. Luminescence, Theory, pp. 636–653.
40 A. Deshmukh, S. Bandyopadhyay, A. James and A. Patra, *J. Mater. Chem. C*, 2016, **4**, 4427–4433.
41 H. Liu, C. Xu, Y. Bai, L. Liu, D. Liao, J. Liang, L. Liu and H. Han, *Spectrochim. Acta A*, 2017, **171**, 311-316.
42 J. L. Colon, C.-Y. Yang, A. Clearfield and C. R. Martin, *J. Phys. Chem.*, 1990, **94**, 874-882.
43 J. Yang and M. A. Winnik, *Can. J. Chem.*, 1995, **73**, 1823–1830.
44 J. Liu, Y. Zhong, P. Lu, Y. Hong, J. W. Lam, M. Faisal, Y. Yu, K. S. Wong and B. Z. Tang, *Polym. Chem.*, 2010, **1**, 426–429.
45 C. Nunes, C. Sousa, H. Ferreira, M. Lucio, J. L. Lima, J. Tavares, A. C. da Silva and S. Reis, *J. Environ. Biol.*, 2008, **29**, 733–738.
46 D. K. Singh, P. K. Iyer and P. Giri, *Carbon*, 2012, **50**, 4495–4505.
47 T. A. Beu and A. Farcas, *AIP Conf. Proc.*, 2017, **1916**, 020001.
48 K.A. Curtis, D. Miller, P. Millard, S. Basu, F. Horkay and P. L. Chandran, *PLoS One*, 2016, **11**, e0158147.
49 D. R. Chang, S. Harden and N. Loverro, *J. Macromol. Sci.-Chem.*, 1986, **23**, 801-804.
50 R. Chen, V. D. Ta, F. Xiao, Q. Zhang and H. Sun, *Small*, 2013, **9**, 1052-1057.
51 M. J. Ruedas-Rama and E. A. H. Hall, *Anal. Chem.*, 2010, **82**, 9043–9049.
52 R. V. Benjaminsen, M. A. Mattebjerg, J. R. Henriksen, S. M. Moghimi and T. L. Andresen, *Mol. Ther.*, 2013, **21**, 149–157.
53 Y. Ding, F. Wu, Y. Zhang, X. Liu, E. M. L. D. de Jong, T. Gregorkiewicz, X. Hong, Y. Liu, M. C. G. Aalders, W. J. Buma and H. Zhang, *J. Phys. Chem. Lett.*, 2015, **6**, 2518-2523.
54 T. Wu, J.-C. Boyer, M. Barker, D. Wilsonn and N. R. Branda, *Chem. Mater.*, 2013, **25**, 2495-2502.
55 L. M. Wiesholler and T. Hirsch, *Opt. Mater.*, 2018, **80**, 253–264.
56 A. Sedlmeier and H. H. Gorris, *Chem. Soc. Rev.*, 2015, **44**, 1526–1560.